Physics of Plasmas ARTICLE scitation.org/journal/php

Verification of local electrostatic gyrokinetic simulation of driftwave instability in field-reversed configuration

Cite as: Phys. Plasmas **27**, 112504 (2020); doi: 10.1063/5.0020288
Submitted: 1 July 2020 · Accepted: 15 October 2020 ·
Published Online: 4 November 2020

Shuying Sun,[1] Xishuo Wei,[2] Zhihong Lin,[2,a)] Pengfei Liu,[2] Wenhao Wang,[2] and Huasheng Xie[3,4]

AFFILIATIONS

[1]Fusion Simulation Center, Peking University, Beijing 100871, China
[2]Department of Physics and Astronomy, University of California, Irvine, California 92697, USA
[3]Hebei Key Laboratory of Compact Fusion, Langfang 065001, China
[4]ENN Science and Technology Development Co. Ltd., Langfang 065001, China

[a)]Author to whom correspondence should be addressed: zhihongl@uci.edu

ABSTRACT

Local linear simulations of ion temperature gradient (ITG) instabilities using a gyrokinetic particle code GKD1D have been verified by comparing with the analytic dispersion relation in the slab geometry and by benchmarking with a global gyrokinetic code GTC-X in a realistic field-reversed configuration (FRC). Results of ITG simulations using either adiabatic or kinetic electrons exhibit excellent agreements between the two codes for linear frequencies, growth rates, and mode structures. The ITG modes in the FRC scrape-off layer region are mostly dominated by the poloidal $m = 1$ harmonic. Kinetic electrons enhance the subdominant $m = 2$ harmonic and the even parity dominates the ITG mode structure. Kinetic electrons increase the growth rates for the low-n modes, but decrease the growth rates for the high-n modes.

I. INTRODUCTION

A field-reversed configuration (FRC) is an elongated compact toroid with an equilibrium magnetic field predominately along the poloidal direction.[1,2] The FRC consists of two topologically different regions that are separated by a magnetic separatrix: an inner core with closed field lines and an outer scrape-off layer (SOL) with open field lines. The FRC has many advantages as a promising fusion reactor candidate. Recent experimental advances in suppressing the macro-instabilities (including rotational, wobble, and tilt modes)[3,4] have successfully raised the confinement time of the FRC plasma to a turbulent transport-limited regime.

Therefore, a comprehensive understanding of the transport process in the FRC plasma has become a high priority, which has motivated recent experimental and computational studies of low frequency driftwave turbulence. The experimental measurements showed that ion-scale fluctuations are absent or strongly suppressed in the FRC core, while ion- and electron-scale turbulences are present in the SOL once a critical pressure gradient is exceeded.[5] These experimental observations have been confirmed in numerical simulations. Linear local electrostatic gyrokinetic particle-in-cell (PIC) simulations using the GTC code found that the ion scale driftwaves in the core are stable and that both ion and electron scale driftwaves are unstable in the SOL.[6] The instability threshold calculated from simulations is consistent with the critical gradient determined from the experimental measurements.[7,8] More recently, nonlinear electrostatic simulations including the separatrix by the global ANC code[9] found that ion-scale driftwave instabilities are linearly unstable in the SOL and nonlinearly spread into the core plasmas. The toroidal wavenumber spectrum from the simulations in the steady state is consistent with experimental measurements. Furthermore, linear global electrostatic simulations using the GTC-X code found that the unstable driftwaves in the SOL exhibit an axially varying structure that is the strongest in the formation exit areas with a bad magnetic curvature.[10]

The global gyrokinetic PIC simulations[9,10] have incorporated comprehensive physics, especially the geometry coupling between the FRC core and SOL, and have provided important insights into driftwave instabilities and turbulent transport in FRC plasmas. However, global simulations are computationally expensive and so would not be

efficient for a large number of simulations. To complement these global codes, a local gyrokinetic code capturing essential physics of driftwave instabilities in the FRC could be an efficient tool for rapid parameter scans and as a first-principles module in a reduced transport model for assessing FRC confinement properties. Although the ratio of kinetic pressure to magnetic pressure $\beta \simeq 1$ in the FRC core, an electrostatic model is suitable for describing the driftwave turbulence in the SOL, where $\beta \ll 1$ due to the stronger magnetic field and lower plasma density and temperature.

In this paper, we report verification of a one-dimensional electrostatic gyrokinetic PIC code GKD1D[11,12] upgraded for radially local simulation of a single toroidal mode number n on a flux surface in the FRC geometry. We first show that linear frequencies and growth rates from GKD1D simulations of ion temperature gradient (ITG) instabilities in a small FRC domain are nearly identical to the analytic dispersion relationship in the slab limit. We then perform a careful benchmark between GKD1D and GTC-X for the ITG instabilities in a realistic SOL geometry of a model FRC. Results of simulations using either adiabatic or kinetic electrons exhibit excellent agreements between the two codes for linear frequencies, growth rates, and mode structures. The ITG modes are mostly dominated by the poloidal $m = 1$ harmonics. Kinetic electrons increase the growth rates for the low toroidal n modes, but decrease the growth rates for the high-n modes. Kinetic electrons can excite the subdominant $m = 2$ harmonics. The mode structures can show both odd and even parities when using adiabatic electrons, while all the mode structures are dominated by even parities with kinetic electrons.

This paper is organized as follows. In Sec. II, we describe the formulation of the linear electrostatic gyrokinetic simulation model, the implementation of various operators, and the equilibrium geometry used in the GKD1D code. We verify the linear GKD1D ITG simulations using an analytic dispersion relationship in the slab limit in Sec. III. We then perform the benchmark of ITG simulations in the FRC geometry between GKD1D and GTC-X codes in Sec. IV. We give a summary and discussion in Sec. V.

II. LOCAL LINEAR GYROKINETIC SIMULATION MODEL OF GKD1D

The GKD1D code is a 1D electrostatic gyrokinetic PIC code using the δf scheme[13,14] to reduce the numerical noise. It was originally developed for a dipole configuration[11,12] and is upgraded in this work for the FRC geometry.

A. Formulation of the simulation model

When considering the ion-scale and electron-scale microturbulence in the FRC under the assumption of low frequency and long parallel wavelength $\omega/\Omega_s \sim \rho_s/L \sim k_\parallel/k_\perp \ll 1$ but short perpendicular wavelength $k_\perp\rho_s \sim 1$, the linear gyrokinetic model[15–17] can be applied. Here, ω is the real frequency of the unstable drift-wave mode and Ω_s and ρ_s are the particle cyclotron frequency and Larmor radius of species "s," respectively. L is the scale length of equilibrium quantities, $k_\perp$ and $k_\parallel$ are the wave numbers in the direction perpendicular and parallel to the magnetic field, respectively. Although the equilibrium distribution function in the mirror-like magnetic field in the SOL should be calculated from an equilibrium model, for simplicity, we assume in this work that the equilibrium is a Maxwellian distribution function $F_{0s} = n_{0s}(m_s/2\pi T_s)^{3/2} e^{-m_s\epsilon/T_s}$, where $\epsilon = v^2/2$, $\mu = v_\perp^2/2B$ is the magnetic moment, $T_s = mv_s^2$ is the particle temperature, and v_s is the species' thermal velocity; the appropriate gyroaveraged perturbed particle distribution function of species "s" is

$$f_s = \frac{q_s}{m_s}\frac{\partial F_{0s}}{\partial \epsilon}\phi + J_0(k_\perp\rho)h_s, \tag{1}$$

with the nonadiabatic perturbed gyrocenter distribution function h_s determined by

$$\left(\omega - \omega_{Ds} + iv_\parallel \boldsymbol{b}\cdot\nabla\right)h_s = -(\omega - \omega_{*s})\frac{\partial F_{0s}}{\partial \epsilon}\frac{q_s}{m_s}J_0\phi. \tag{2}$$

Here, J_0 is the Bessel function of the first kind, $\mathbf{b} = \mathbf{B}/B$, with $\mathbf{B}$ being the magnetic field and q_s and m_s being the charge and mass of species "s," respectively. The diamagnetic drift frequency ω_{*s} and the magnetic drift frequency ω_{Ds} are expressed as

$$\omega_{*s} = \frac{\boldsymbol{k}_\perp \times \boldsymbol{b}\cdot\nabla F_{0s}}{-\Omega_s \partial F_{0s}/\partial\epsilon} = \frac{\boldsymbol{k}_\perp \times \boldsymbol{b}\cdot\nabla F_{0s}}{q_s B F_{0s}/T_s}, \tag{3}$$

$$\omega_{Ds} = \boldsymbol{k}_\perp \cdot \boldsymbol{v}_d = \boldsymbol{k}_\perp \cdot \boldsymbol{b} \times \frac{\mu\nabla B + v_\parallel^2 \boldsymbol{b}\cdot\nabla\boldsymbol{b}}{\Omega_s}. \tag{4}$$

For the initial value simulation method, we can remove the ω term on the righthand side of Eq. (2) by defining

$$g_s \equiv h_s - \frac{q_s}{T_s}F_{0s}J_0\phi, \quad \text{i.e., } f_s = -\frac{q_s}{T_s}F_{0s}\left(1 - J_0^2\right)\phi + J_0 g_s, \tag{5}$$

and Eq. (2) changes to (with definition of $\mathbf{b}\cdot\nabla = \partial/\partial l$, $\omega = i\partial/\partial t$)

$$\left(\frac{\partial}{\partial t} + v_\parallel\frac{\partial}{\partial l}\right)g_s = -i\omega_{Ds}g_s - i(\omega_{Ds} - \omega_{*s})\frac{q_s}{T_s}F_{0s}J_0\phi - v_\parallel\frac{q_s}{T_s}F_{0s}\left[J_0\frac{\partial}{\partial l}\phi - \phi J_1\frac{\partial}{\partial l}(k_\perp\rho)\right], \tag{6}$$

where we have used $J_0' = -J_1$.

For electrostatic perturbations, the gyrokinetic equation is closed by the Poisson equation

$$\sum_s q_s \int f_s d^3v = 0, \tag{7}$$

and by substituting Eq. (5), this equation for a two-species plasma reads

$$-\frac{q_i n_i}{T_i}(1 - \Gamma_{0i})\phi + \int J_0 g_i d^3v = -\frac{q_e n_e}{T_e}(1 - \Gamma_{0e})\phi + \int J_0 g_e d^3v, \tag{8}$$

where $\Gamma_{0s} \equiv I_0(b_s)e^{-b_s}$ and $b_s = (k_\perp\rho_s)^2$.

In the δf-scheme, we define the weight of the perturbed distribution $w_s = g_s/F_{0s}$. Equation (6) can be written as

$$\frac{dw_s}{dt} \equiv \left(\frac{\partial}{\partial t} + v_\parallel\frac{\partial}{\partial l}\right)w_s = -i\omega_{Ds}w_s - i(\omega_{Ds} - \omega_{*s})\frac{q_s}{T_s}J_0\phi - v_\parallel\frac{q_s}{T_s}\left[J_0\frac{\partial\phi}{\partial l} - \phi J_1\frac{\partial}{\partial l}(k_\perp\rho)\right], \tag{9}$$

and the quasi-neutrality Eq. (8) now yields

$$\left[\frac{q_i n_i}{T_i}(1-\Gamma_{0i})-\frac{q_e n_e}{T_e}\right]\phi=\int J_0 g_i d^3v-\int J_0 g_e d^3v. \quad (10)$$

Here, the finite Larmor radius (FLR) effects are kept for ions, but are neglected for electrons in all simulations of ion scale instabilities reported in this paper. The guiding center equations of motion [i.e., propagator on the left-hand-side of Eq. (9)] for the linear local simulation are

$$\frac{dl}{dt}=v_{\parallel}, \quad (11)$$

$$\frac{dv_{\parallel}}{dt}=\frac{dv_{\parallel}}{dl}\frac{dl}{dt}=\frac{d}{dl}\frac{v_{\parallel}^2}{2}=-\mu\frac{dB}{dl}. \quad (12)$$

The perturbed electric field does not appear in Eq. (12) since only unperturbed orbits are used in the linear simulation. Equations (9)–(12) constitute the final equation system we solve for local electrostatic linear driftwave instabilities in an FRC.

B. Implementation of operators

When solving for Eqs. (9) and (10), we need to calculate $\partial/\partial l$, $v_{\parallel}$, $\partial(k_{\perp}\rho)/\partial l$, ω_{*s}, ω_{Ds}, and b_s. Here, we describe the implementation of these terms in the GKD1D code.

The flux coordinates $(\psi,\ \theta,\ \zeta)$ are used in the GKD1D, where $\psi=\psi(r,\ z)$ is the magnetic flux function, $\theta=\theta(r,\ z)$ is the poloidal (parallel) coordinate, $\zeta=-\varphi$ is the toroidal angle, and $(r,\ \varphi,\ z)$ are the cylindrical coordinates. An ideal FRC has a purely poloidal equilibrium magnetic field, which enables us to write

$$\boldsymbol{B}=-\nabla\psi\times\nabla\zeta,$$
$$k_{\perp}=k_{\psi}\hat{\boldsymbol{e}}_{\psi}+k_{\zeta}\hat{\boldsymbol{e}}_{\zeta}.$$

In this coordinate definition, $\hat{\boldsymbol{e}}_{\zeta}$ is in the ion diamagnetic drift direction and $\hat{\boldsymbol{e}}_{\psi}$ is the direction perpendicular to the flux surface. Although there is no toroidal coupling due to the zero magnetic shear in the FRC, the driftwave eigenmode often forms a radially elongated structure ($k_{\psi}\ll k_{\zeta}$) to minimize the finite Larmor radius effects as observed in the ANC simulation.[9] Since we aim to implement a local simulation model, all variations in the radial direction can be ignored and we simply take $k_{\psi}=0$ and $k_{\perp}=k_{\zeta}=n/r$, where n is the toroidal mode number. Then, we have

$$k_{\perp}\rho_s=\frac{nm_s v_s}{q_s}\frac{1}{rB},\quad b_s=\left(\frac{nm_s v_s}{q_s}\frac{1}{rB}\right)^2. \quad (13)$$

In order to unify the local simulation along a magnetic field line for both the core and the SOL regions of the FRC, which are topologically different, we express the differential operator along the magnetic field line dl as $dl=R_0\kappa d\theta$, where $\kappa(\psi)$ is a function that maps the parallel distance to an angle-like poloidal coordinate $\theta\in[-\pi,\ \pi]$. As a result,

$$\frac{\partial}{\partial l}=\frac{1}{R_0\kappa}\frac{\partial}{\partial\theta}. \quad (14)$$

Considering μ conservation and $v_{\parallel}=dl/dt$, we have

$$\frac{\partial}{\partial\theta}(k_{\perp}\rho)=-\frac{nm_s}{q_s}\frac{\sqrt{2\mu}}{\alpha^2}\left(\frac{\partial\alpha}{\partial\theta}\right)_{\psi=\psi_1}, \quad (15)$$

$$\frac{d\theta}{dt}=\frac{v_{\parallel}}{R_0\kappa}, \quad (16)$$

where we define $\alpha\equiv r\sqrt{B}$.

For a typical FRC equilibrium, we can express $n_0=n_0(\psi)$ and $T=T(\psi)$; so, we have

$$\nabla F_{0s}=\left\{\frac{\nabla n_{0s}}{n_{0s}}+\frac{\nabla T_s}{T_s}\left[\frac{m_s\epsilon}{T_s}-\frac{3}{2}\right]\right\}F_{0s}$$
$$=-\frac{\nabla\psi}{\psi_0}\left\{\kappa_{ns}+\kappa_{Ts}\left[\frac{m_s\epsilon}{T_s}-\frac{3}{2}\right]\right\}F_{0s},$$

where $\kappa_{ns}\equiv-\psi_0\partial\ln n_{0s}/\partial\psi$, $\kappa_{Ts}\equiv-\psi_0\partial\ln T_s/\partial\psi$ for each species and $\psi_0=B_0R_0^2$. Insert the upper expression into Eq. (3), and noting that $(\mathbf{k}_{\perp}\times\mathbf{b})\cdot\nabla\psi=[n\nabla\zeta\times\mathbf{b}]\cdot\nabla\psi=-nB$, yields

$$\omega_{*s}=\omega_{d0s}\left\{\kappa_{ns}+\kappa_{Ts}\left[\frac{m_s\epsilon}{T_s}-\frac{3}{2}\right]\right\}, \quad (17)$$

where $\omega_{d0s}\equiv\frac{nT_s}{q_s\psi_0}$.

The $\hat{\boldsymbol{e}}_{\zeta}$ component of gradient drift velocity $\mathbf{v}_g$, curvature drift velocity $\mathbf{v}_c$, and total drift velocity $\mathbf{v}_d$ are

$$\boldsymbol{v}_g\cdot\hat{\boldsymbol{e}}_{\zeta}=\frac{\mu}{\Omega_{cs}}(\boldsymbol{b}\times\nabla B)\cdot\hat{\boldsymbol{e}}_{\zeta}=\frac{\mu Bg(\theta)}{\Omega_s R_0},$$
$$\boldsymbol{v}_c\cdot\hat{\boldsymbol{e}}_{\zeta}=\frac{v_{\parallel}^2}{\Omega_{cs}}(\nabla\times\boldsymbol{b})\cdot\hat{\boldsymbol{e}}_{\zeta}=\frac{2(\epsilon-\mu B)c(\theta)}{\Omega_s R_0},$$
$$\boldsymbol{v}_d\cdot\hat{\boldsymbol{e}}_{\zeta}=(\boldsymbol{v}_g+\boldsymbol{v}_c)\cdot\hat{\boldsymbol{e}}_{\zeta}=\frac{1}{\Omega_s R_0}[\mu Bg+2c(\epsilon-\mu B)],$$

where we define $g(\theta)\equiv R_0(\mathbf{b}\times\nabla B)\cdot\hat{\mathbf{e}}_{\zeta}/B$ and $c(\theta)\equiv R_0(\nabla\times\mathbf{b})\cdot\hat{\mathbf{e}}_{\zeta}$. Inserting the upper expression into Eq. (4) yields

$$\omega_{Ds}=\omega_{d0s}\frac{R_0B_0}{rB}\left[\frac{\mu Bg}{v_s^2}+\frac{2c(\epsilon-\mu B)}{v_s^2}\right]. \quad (18)$$

C. Equilibrium and flux line domain

All simulations in this paper use a model FRC geometry reported by earlier GTC simulations.[6–8,18] The FRC magnetic geometry in Boozer coordinates was constructed using equilibrium data from the LR_eqMI code,[19] which is an axisymmetric force balance solver including realistic wall and coil geometry. Figure 1 shows the poloidal magnetic flux ψ contour of this equilibrium, where the black dashed line represents the separatrix between the core and SOL. The

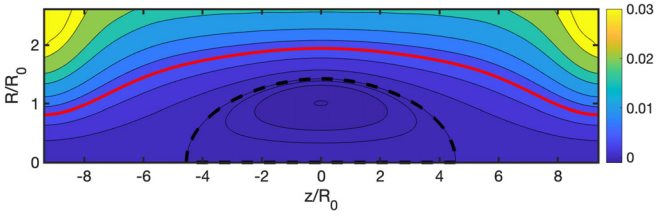

FIG. 1. Contour plot of the magnetic flux function on a poloidal plane of a representative FRC equilibrium.[6–10,18] The red line denotes the flux surface ψ_1 used by all simulations in this paper.

separatrix radius $R_{sep} = 38$ cm is the distance from the cylindrical axis to the separatrix on the $z = 0$ midplane and the major radius $R_0 = 27$ cm is the distance from the cylindrical axis to the null-point on the midplane.

The GKD1D code uses a single flux-surface geometry to study the local linear properties of the FRC core and SOL separately. Since the ion scale driftwaves are more easily driven unstable in the SOL, the verification is done at a single flux surface which passes through $(r, z) = (1.93, 0)R_0$ (the red line shown in Fig. 1). The magnetic field at the point of $z = 0$ on this flux surface is $B_1 = 966$ G. The ratio of kinetic pressure to magnetic pressure $\beta = 0.021 \ll 1$ on this flux surface, which justifies the electrostatic simulation model described in this work. This flux surface is chosen to be at the maximal mode amplitude of the ion-scale instabilities in previous simulations by GTC,[6–8] GTC-X,[10] and ANC[9] codes using model plasma profiles.[5] The turbulences driven at this SOL location can spread across the separatrix and cause transport in the FRC core.[9] In the parallel direction, only the segment between $z/R_0 = [-9.33, 9.33]$ is used. This segment is chosen because the whole FRC core can be included in a global simulation and the magnetic field is roughly parallel to the z-axis at the boundary for applying periodic boundary conditions in the parallel direction. The finite difference method is applied in the parallel direction. In the toroidal direction, a single toroidal mode number n is selected using the spectral method to simplify the flux surface into a field line. Although the neutral beam injection (NBI) may be extensively applied in the modern FRC, the NBI's contribution to the driftwave instabilities is not considered in this work, because the NBI ions cannot be simulated by the gyrokinetic model.

Before verifying the dispersion relation and benchmarking with the GTC-X code, the numerical convergence of the upgraded GKD1D code has been studied with regard to particle convergence, space grid convergence, and time step convergence, respectively. This is done based on a typical case of the following equilibrium: $T_i = T_e = 80$ eV, $\kappa_{ni} = \kappa_{ne} = 0.71$, $\kappa_{Ti} = 1.42$, $\kappa_{Te} = 0.00$, $n = 20$, $k_r = 0$, and deuterium ions. Table I shows several characteristic length scales at the simulation location. The ion gyroradius is much smaller than the equilibrium length scales, which corroborated the validity of the gyrokinetic model applied to this FRC simulation. The variations of simulation results decrease to <0.5% when using $n_{part}/n_{grid} = 1600$, $n_{grid} = 64$, $\Delta t = 0.005\, c_s/R_0$, where $c_s = \sqrt{T_e/m_i}$ is the sound velocity, which will be used in all following simulations. The characteristic lengths of plasma profiles and magnetic fields are listed in Table I to justify the conservation of the magnetic moment and the gyrokinetic simulation model.

III. VERIFICATION OF GKD1D USING THE ANALYTIC DISPERSION RELATION

In the slab geometry, the gyrokinetic model Eqs. (9) and (10) can readily be solved for $k_\parallel = 0$ modes, yielding the following integral dispersion relation:

TABLE I. Characteristic lengths (unit: cm) used in the simulations. L_{Ti} and L_n are the ion temperature and density scale length, respectively. ρ_i is the ion gyroradius. L_B and R_c are, respectively, the scale length and inverse of the curvature of the magnetic field.

L_{Ti}	L_n	ρ_i	L_B	R_c
5.4	10.8	1.3	81.2	141

$$\sum_{s=i,e} \frac{1}{T_s}\left[1 - \int \frac{\omega - \omega_{*s}}{\omega - \omega_{Ds}} J_0^2 F_{0s} d^3v\right] = 0. \tag{19}$$

For the Maxwellian distribution function, $F_{0s} = (m_s/2\pi T_s)^{3/2} e^{(-m_s v^2/2T_s)}$; this yields the dispersion relation

$$D(\omega, k_\perp) = \sum_{s=i,e} \frac{1}{T_s}\left[1 - \frac{1}{\sqrt{2\pi}} \int \frac{\omega - \omega_{*s}}{\omega - \omega_{Ds}} J_0^2(k_\perp \rho) \times \exp\left(-\frac{y^2}{2}\right) y_\perp dy_\perp dy_\parallel\right] = 0, \tag{20}$$

where $y = v/v_s, y_\perp = v_\perp/v_s, y_\parallel = v_\parallel/v_s$. For an adiabatic electron model, Eq. (20) reduced to

$$\frac{1}{T_i}\left[1 - \frac{1}{\sqrt{2\pi}} \int \frac{\omega - \omega_{*i}}{\omega - \omega_{Di}} J_0^2(k_\perp \rho) \exp\left(-\frac{y^2}{2}\right) y_\perp dy_\perp dy_\parallel\right] + \frac{1}{T_e} = 0. \tag{21}$$

The accuracy of the GKD1D code is verified using this theoretical dispersion relation. By limiting the parallel domain to a small size of $z = [-0.05, 0.05]R_0$ and applying periodic boundary conditions in the parallel direction, we can regard the resulted configuration as a slab geometry and thereby compare the simulation results with the Eqs. (20) and (21) solved by the mgk0d code implemented in MATLAB.[11] We show the comparison for the adiabatic electron case in Fig. 2 for a large range of toroidal mode numbers $n = [25, 60]$, which corresponds to $k_\perp \rho_i = [0.91, 2.18]$. The comparison for the kinetic electron case is shown in Fig. 3 for a range of toroidal mode numbers $n = [60, 120]$, which corresponds to $k_\perp \rho_i = [3.45, 6.91]$. All modes are dominated by the $k_\parallel = 0$ component, consistent with the assumption of Eq. (20). The simulation results show excellent agreement with analytic theory, which gives a verification of the GKD1D simulations.

IV. BENCHMARK BETWEEN GKD1D AND GTC-X

In this section, the GKD1D code is benchmarked with the Gyrokinetic Toroidal Code-X (GTC-X code),[10] which has been developed using many advanced physics and numerical capabilities from GTC[20] and is specially developed for nonlinear global simulations of

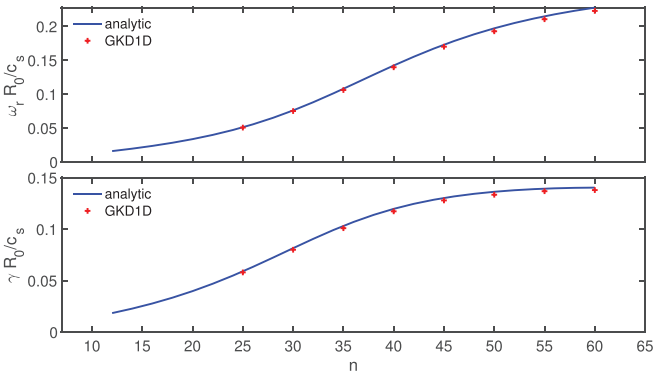

FIG. 2. ITG linear frequency (ω_r) and growth rate (γ) comparison between the GKD1D simulation results and the analytic dispersion relation for different mode numbers (n) using an adiabatic electron model.

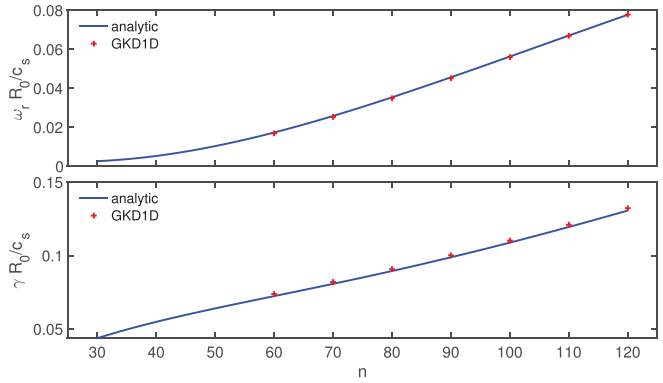

FIG. 3. ITG linear frequency (ω_r) and growth rate (γ) comparison between the GKD1D simulation results and the analytic dispersion relation for different mode numbers (n) using the kinetic electron model.

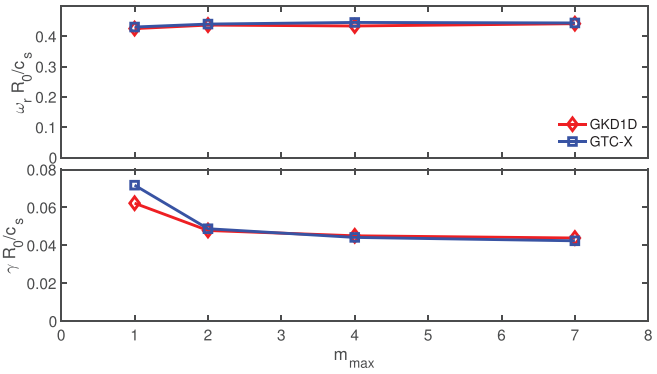

FIG. 4. Dependence of ITG linear frequency (ω_r) and growth rate (γ) on the maximal poloidal harmonics (m_{max}) kept in simulations. Each simulation keeps n = 24 and m = [0, m_{max}] harmonics. The case for $m_{max} = 0$ is stable.

the FRC[10] and tokamak[21] including magnetic separatrix using cylindrical coordinates.

In order to benchmark with the 1D gyrokinetic PIC code GKD1D, we make some simplifications in the simulation model of the 3D gyrokinetic PIC code GTC-X. First, we limit the GTC-X simulation radial domain to the vicinity of the selected flux surface ψ_1 (the red line shown in Fig. 1) in the GKD1D simulation, i.e., the GTC-X simulation radial domain is $\psi = [0.998,\ 1.002]\psi_1$. Second, a single toroidal n mode is selected using a spectral method in the GTC-X simulations. The parallel domain is also identical in the two codes. The simulation domain used by these two codes is confirmed by comparing the difference of several important equilibrium variables, e.g., B, $\nabla B/B$, $\nabla n/n$, and $\nabla T/T$, all of which give a relative difference of less than 2%. The main discrepancy comes from the different types of discretization in parallel coordinates implemented in the two codes.

Since the ITG parallel wavelength is expected to be much longer than the perpendicular wavelength, we first perform convergence studies on the number of poloidal harmonics needed to represent the ITG eigenmode. The simulation parameters are listed here: $T_i = T_e = 80$ eV, $\kappa_{ni} = \kappa_{ne} = 0.71$, $\kappa_{Ti} = 1.42$, $\kappa_{Te} = 0.00$, n = 20, $k_r = 0$, and deuterium ions. A parallel mode filter is implemented in both GKD1D and GTC-X to select the poloidal harmonics kept in the simulations to be m = [0, m_{max}]. The linear simulation results using gyrokinetic electrons for the convergence with respect to m_{max} are shown in Fig. 4 for both GKD1D and GTC-X, which agree very well. The case for $m_{max} = 0$ is stable. It can be seen in Fig. 4 that the real frequency and growth rate of the n = 24 ITG mode show almost no changes when m_{max} increases from 2 to 7, which suggests that the dominant parallel harmonics are m = 0, 1, 2. Therefore, only the parallel harmonics of m = [0, 4] are kept in the following simulations. The ITG eigenmodes are formed by linear couplings of these poloidal harmonics because of variations in the magnetic field amplitude along the field line with dominant poloidal harmonics m = 0, 1, 2.

The results of linear ITG simulations by GKD1D and GTC-X using adiabatic electrons are compared in Fig. 5 with the toroidal mode n = [12, 36], which corresponds to $k_\perp \rho_i = [0.44, 1.31]$. Figures 5(a) and 5(b) show that both the real frequencies and the growth rates from these two codes agree very well with a relative difference less than 5%. These are weak ITG instabilities propagating in the ion diamagnetic direction with $\gamma/\omega_r < 20\%$. Figure 5(c) shows that these two codes give a nearly identical ITG parallel mode structure of the electrostatic potential for the n = 24 case. These ITG eigenmodes are odd with respect to the outer midplane (z = 0 or $\theta = 0$) and dominated by the m = 1 harmonics.

The linear results of ITG simulations by GKD1D and GTC-X using kinetic electrons show that kinetic electrons increase the growth rate of the low-n modes (n = 12 and 16), but decrease the growth rate for high-n modes (n ≥ 20). The modes still propagate in the ion diamagnetic direction similar to that in the adiabatic electron cases.

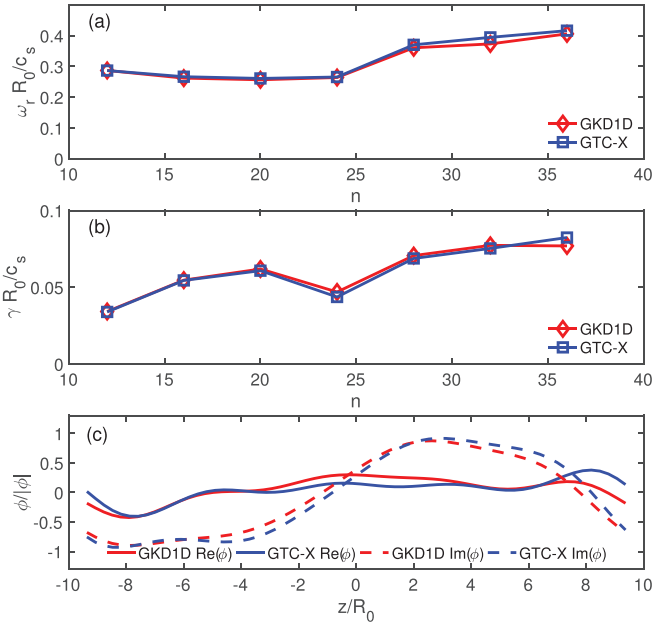

FIG. 5. Comparison of GKD1D and GTC-X simulation results using adiabatic electrons. (a) Dependence of ITG linear frequency (ω_r) on the toroidal mode number (n), (b) dependence of ITG growth rate (γ) on the toroidal mode number (n), and (c) real (solid lines) and imaginary (dashed lines) part of electrostatic potential (ϕ) for the n = 24 ITG mode as a function of the parallel coordinate (z).

Figures 6(a) and 6(b) show good agreement for the real frequency and the growth rate with a relative error of $\leq 5\%$, except for the n = 20 case. The difference in the real frequency of the n = 20 case from these two codes seems to be related to the difference in the eigenmode structure: the m = 1 harmonics dominates in the GKD1D simulation, but the m = 2 harmonics dominates in the GTC-X simulation of the n = 20 mode. For all other n modes, the m = 1 harmonics dominates in both GKD1D and GTC-X simulations. For example, the n = 24 ITG parallel mode structures of the electrostatic potential are shown in Fig. 6(c), which demonstrates very good agreements between these two codes. But the mode structure changes to even parity, i.e., symmetric with respect to the outer midplane (z = 0 or $\theta = 0$) in this case, compared to the odd parity, i.e., antisymmetric with respect to the outer midplane, in the adiabatic electron case [Fig. 5(c)]. Comparison of Figs. 5(c) and 6(c) shows that amplitudes of the m = 2 harmonics in the simulations using kinetic electrons are significantly higher than those in the simulations using adiabatic electrons.

We list the parity of the ITG eigenmodes for toroidal modes n = [12, 36] using both the adiabatic electron model and the kinetic electron model in Table II. These two codes produce identical parities for the mode structures of the electrostatic potential. Interestingly, the mode structures show both odd and even parities when using adiabatic electrons, while all the mode structures only show even parities with kinetic electrons. We have tested different initial perturbations and found that the results in Table II are robust. Since the magnetic geometry is nearly up-down symmetric, the growth rates of even parity and odd parity modes should be similar. We conjecture that the small up-down asymmetry of the magnetic geometry breaks the symmetry between the odd and even modes.

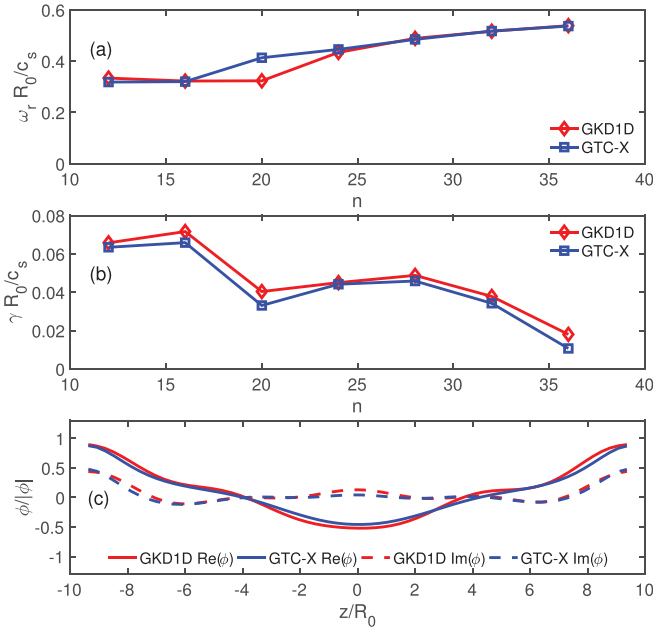

FIG. 6. Comparison of GKD1D and GTC-X simulation results using kinetic electrons. (a) Dependence of ITG linear frequency (ω_r) on the toroidal mode number (n), (b) dependence of growth rate (γ) on the toroidal mode number (n), and (c) real (solid lines) and imaginary (dashed lines) parts of electrostatic potential (ϕ) for the n = 24 ITG mode as a function of the parallel coordinate (z).

TABLE II. Parity for ITG mode structures of electrostatic potential for various toroidal mode numbers with adiabatic or kinetic electrons.

	Adiabatic electrons		Kinetic electrons	
Toroidal mode ***n***	GKD1D	GTC-X	GKD1D	GTC-X
12	Even	Even	Even	Even
16	Even	Even	Even	Even
20	Even	Even	Even	Even
24	Odd	Odd	Even	Even
28	Odd	Odd	Even	Even
32	Odd	Odd	Even	Even
36	Even	Even	Even	Even

To clarify the effects of kinetic electrons on the ITG mode structure, we have simulated each toroidal mode n with a single poloidal harmonic of m = 1 or m = 2. Figure 7 shows the dependence of the linear frequency and growth rate for each (m, n) harmonic from simulations using the GKD1D with adiabatic or kinetic electrons. The m = 2 harmonic is stable for adiabatic electrons, but is unstable for kinetic electrons, especially for $n \leq 24$ modes. The growth rate of the m = 2 harmonic is smaller than that of the m = 1 harmonic for all toroidal mode numbers. This explains the results in Figs. 5 and 6 that the m = 2 harmonic is significantly enhanced with kinetic electrons, but the mode structure is still dominated by the m = 1 harmonic. For the n = 20 mode, the growth rates of the two harmonics are close to each other and the amplitudes of the two harmonics are similar, so that the m = 1 harmonic dominates in the GKD1D simulation but the m = 2 harmonic dominates in the GTC-X simulation. Since magnetic field amplitude variations along the field line contain a significant component of the m = 2 harmonic, the perturbation with the m = 2 harmonic is likely excited by trapped electrons, as all frequencies are much smaller than the electron bounce frequency. The perturbation with the m = 2 harmonic would presumably prefer an even parity due to the bounce-average by the trapped electrons. This could lead to

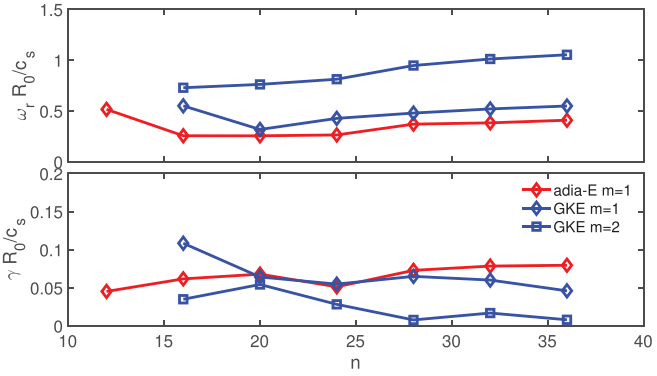

FIG. 7. Dependence of ITG linear frequency (ω_r) and growth rate (γ) on the toroidal mode number (n) from GKD1D simulations using a single poloidal harmonic m = 1 or m = 2 with adiabatic or kinetic electrons.

a preferred even parity of the ITG mode structure because of the coupling between the m = 1 and m = 2 harmonics.

V. SUMMARY AND DISCUSSION

In this paper, we report the implementation and verification of a one-dimensional gyrokinetic PIC code GKD1D upgraded for efficient local simulation of FRC geometry. We show that linear frequencies and growth rates from GKD1D simulations of ion temperature gradient (ITG) instabilities in a small FRC domain are nearly identical to the analytic dispersion relationship in the slab limit. We perform a careful benchmark between GKD1D and GTC-X for the ITG instabilities in a realistic SOL geometry of a model FRC. Results of simulations using either adiabatic or kinetic electrons exhibit excellent agreements between the two codes for linear frequencies, growth rates, and mode structures. The ITG mode structures are mostly dominated by the poloidal m = 1 harmonic. The subdominant m = 2 harmonic can be excited by kinetic electrons. Kinetic electrons also increase the growth rates for the low toroidal n modes, but decrease the growth rates for the high-n modes. The mode structures show both odd and even parities when using adiabatic electrons, while all the mode structures only show even parities with kinetic electrons.

The successful benchmark between GKD1D and GTC-X reported in this paper has verified an efficient local simulation model for driftwave instability in the FRC, which will be utilized for parameter scans and sensitivity studies of confinement properties in existing FRC experiments and in the design of future FRC experiments. The current simulations also extend our earlier simulations[11] of the long wavelength ITG instability in the FRC SOL to including effects of kinetic electrons.

In future work, a fully kinetic ion simulations model[22] will be implemented to study the effects of fast ions on the driftwave instabilities.

ACKNOWLEDGMENTS

The authors would like to thank Dr. Sean Dettrick, Dr. Laura Galeotti, Dr. Calvin Lau, and Dr. Jian Bao for providing the equilibrium data shown in Fig. 1. This work was supported by the China National Magnetic Confinement Fusion Science Program (Grant Nos. 2018YFE0304100 and 2017YFE0301303), the ENN Science and Technology Development Co. Ltd., and the U.S. DOE Scientific Discovery through the Advanced Computing (SciDAC) program under Award No. DE-SC0018270 (SciDAC ISEP Center). Part of the work was done while Shuying Sun was working at ENN. GKD1D simulations were performed on the High Performance Computing Platform of Peking University, China and the computational resources of ENN. GTC-X simulations used resources on the Oak Ridge Leadership Computing Facility at Oak Ridge National Laboratory (DOE Contract No. DE-AC05-00OR22725) and the National Energy Research Scientific Computing Center (DOE Contract No. DE-AC02-05CH11231).

DATA AVAILABILITY

The data that support the findings of this study are available from the corresponding author upon reasonable request.

REFERENCES

[1]L. C. Steinhauer, Phys. Plasmas **18**, 070501 (2011).
[2]M. Tuszewski, Nucl. Fusion **28**, 2033 (1988).
[3]M. W. Binderbauer, T. Tajima, L. C. Steinhauer, E. Garate, M. Tuszewski, L. Schmitz, H. Y. Guo, A. Smirnov, H. Gota, D. Barnes, B. H. Deng, M. C. Thompson, E. Trask, X. Yang, S. Putvinski, N. Rostoker, R. Andow, S. Aefsky, N. Bolte, D. Q. Bui, F. Ceccherini, R. Clary, A. H. Cheung, K. D. Conroy, S. A. Dettrick, J. D. Douglass, P. Feng, L. Galeotti, F. Giammanco, E. Granstedt, D. Gupta, S. Gupta, A. A. Ivanov, J. S. Kinley, K. Knapp, S. Korepanov, M. Hollins, R. Magee, R. Mendoza, Y. Mok, A. Necas, S. Primavera, M. Onofri, D. Osin, N. Rath, T. Roche, J. Romero, J. H. Schroeder, L. Sevier, A. Sibley, Y. Song, A. D. Van Drie, J. K. Walters, W. Waggoner, P. Yushmanov, and K. Zhai, Phys. Plasmas **22**, 056110 (2015).
[4]H. Gota, M. W. Binderbauer, T. Tajima, S. Putvinski, M. Tuszewski, B. H. Deng, S. A. Dettrick, D. K. Gupta, S. Korepanov, R. M. Magee, T. Roche, J. A. Romero, A. Smirnov, V. Sokolov, Y. Song, L. C. Steinhauer, M. C. Thompson, E. Trask, A. D. Van Drie, X. Yang, P. Yushmanov, K. Zhai, I. Allfrey, R. Andow, E. Barraza, M. Beall, N. G. Bolte, E. Bomgardner, F. Ceccherini, A. Chirumamilla, R. Clary, T. DeHaas, J. D. Douglass, A. M. DuBois, A. Dunaevsky, D. Fallah, P. Feng, C. Finucane, D. P. Fulton, L. Galeotti, K. Galvin, E. M. Granstedt, M. E. Griswold, U. Guerrero, S. Gupta, K. Hubbard, I. Isakov, J. S. Kinley, A. Korepanov, S. Krause, C. K. Lau, H. Leinweber, J. Leuenberger, D. Lieurance, M. Madrid, D. Madura, T. Matsumoto, V. Matvienko, M. Meekins, R. Mendoza, R. Michel, Y. Mok, M. Morehouse, M. Nations, A. Necas, M. Onofri, D. Osin, A. Ottaviano, E. Parke, T. M. Schindler, J. H. Schroeder, L. Sevier, D. Sheftman, A. Sibley, M. Signorelli, R. J. Smith, M. Slepchenkov, G. Snitchler, J. B. Titus, J. Ufnal, T. Valentine, W. Waggoner, J. K. Walters, C. Weixel, M. Wollenberg, S. Ziaei, L. Schmitz, Z. Lin, A. A. Ivanov, T. Asai, E. A. Baltz, and J. C. Platt, Nucl. Fusion **59**, 112009 (2019).
[5]L. Schmitz, D. P. Fulton, E. Ruskov, C. Lau, B. H. Deng, T. Tajima, M. W. Binderbauer, I. Holod, Z. Lin, H. Gota, M. Tuszewski, S. A. Dettrick, and L. C. Steinhauer, Nat. Commun. **7**, 13860 (2016).
[6]D. P. Fulton, C. K. Lau, I. Holod, Z. Lin, and S. Dettrick, Phys. Plasmas **23**, 012509 (2016).
[7]D. P. Fulton, C. K. Lau, L. Schmitz, I. Holod, Z. Lin, T. Tajima, and M. W. Binderbauer, Phys. Plasmas **23**, 056111 (2016).
[8]C. K. Lau, D. P. Fulton, I. Holod, Z. Lin, M. Binderbauer, T. Tajima, and L. Schmitz, Phys. Plasmas **24**, 082512 (2017).
[9]C. K. Lau, D. P. Fulton, J. Bao, Z. Lin, T. Tajima, L. Schmitz, and S. Dettrick, Nucl. Fusion **59**, 066018 (2019).
[10]J. Bao, C. K. Lau, Z. Lin, H. Y. Wang, D. P. Fulton, S. Dettrick, and T. Tajima, Phys. Plasmas **26**, 042506 (2019).
[11]H. S. Xie, Y. Y. Li, Z. X. Lu, W. K. Ou, and B. Li, Phys. Plasmas **24**, 072106 (2017).
[12]H. Xie, Y. Zhang, Z. Huang, W. Ou, and B. Li, Phys. Plasmas **24**, 122115 (2017).
[13]S. E. Parker and W. W. Lee, Phys. Fluids B **5**, 77 (1993).
[14]T. Tajima, *Computational Plasma Physics: With Applications to Fusion and Astrophysics* (CRC Press, 2018).
[15]E. A. Frieman and L. Chen, Phys. Fluids **25**, 502 (1982).
[16]W. W. Lee, Phys. Fluids **26**, 556 (1983).
[17]P. J. Catto, W. M. Tang, and D. E. Baldwin, Plasma Phys. **23**, 639 (1981).
[18]C. Lau, "Electrostatic turbulence and transport in the field-reversed configuration," Ph.D. dissertation (UC Irvine, 2017).
[19]L. Galeotti, D. C. Barnes, F. Ceccherini, and F. Pegoraro, Phys. Plasmas **18**, 082509 (2011).
[20]Z. Lin, T. S. Hahm, W. W. Lee, W. M. Tang, and R. B. White, Science **281**, 1835 (1998).
[21]S. De, T. Singh, A. Kuley, J. Bao, Z. Lin, G. Y. Sun, S. Sharma, and A. Sen, Phys. Plasmas **26**, 082507 (2019).
[22]C. K. Lau, D. P. Fulton, J. Bao, Z. Lin, S. Dettrick, M. Binderbauer, T. Tajima, and L. Schmitz, Phys. Plasmas **27**, 082504 (2020).